Pergamon

Int. J. Heat Mass Transfer. Vol. 40, No. 10, pp. 2307–2325, 1997

0017–9310/97 $17.00+0.00

PII: S0017–9310(96)00303–1

Heat transfer enhancement mechanisms in inline and staggered parallel-plate fin heat exchangers

L. W. ZHANG,† S. BALACHANDAR,‡¶ D. K. TAFTI§ and F. M. NAJJAR§

† Department of Mechanical and Industrial Engineering, ‡ Department of Theoretical and Applied Mechanics and § National Center for Supercomputing Applications, University of Illinois at Urbana-Champaign, Urbana, IL 61801, U.S.A.

(*Received* 31 *May* 1996 *and in final form* 21 *August* 1996)

Abstract—Heat transfer enhancement mechanisms and performance of parallel-plate fin heat exchangers are studied. Geometry effects such as finite fin thickness and inline vs staggered arrangements have been investigated. The time-dependent flow behavior due to vortex shedding has been taken into consideration by solving unsteady equations in two-dimensions. Companion steady symmetrized flow calculations have also been performed to identify the effect of vortices on heat transfer and frictional loss. Additional comparisons have been made with theoretical results for fully developed flow between parallel plates and numerical results for restarted boundary layers to quantify boundary layer restart mechanism. © 1997 Elsevier Science Ltd. All rights reserved.

INTRODUCTION

It has been known from simple theory and experimental results [1–8] that surface interruption can be used for enhancing heat transfer. Some examples which exploit surface interruption are the offset-strip and louvered fin surfaces used widely in compact heat exchangers. Surface interruption enhances heat transfer through two independent mechanisms. First, surface interruption prevents the continuous growth of the thermal boundary layer by periodically interrupting it. Thus the thicker thermal boundary layer in continuous-plate fins, which offers higher thermal resistance to heat transfer, is maintained thin and the resistance to heat transfer is reduced. Previous experimental and numerical studies have shown that this heat transfer enhancement mechanism occurs even at low Reynolds numbers when the flow is steady and laminar [1, 2, 4]. Above a critical Reynolds number, the interrupted surfaces offer an additional mechanism of heat transfer enhancement by inducing oscillations in the flow in the form of shed vortices. These vortices enhance local heat transfer by continuously bringing fresh fluid towards the heat transfer surfaces [9, 10].

In addition to heat transfer enhancement, surface interruption increases the friction loss and thus requires higher pumping power. This is partly due to the higher skin friction associated with the hydrodynamic boundary layer restarting. In addition, in the unsteady flow regime, the time-dependent flow behavior associated with vortex shedding increases frictional loss through the Stokes layer dissipation [7] and form drag through Reynolds stresses [11]. Thus the boundary layer restart and the self-sustained oscillatory mechanisms simultaneously influence both the overall heat transfer and the pumping power requirement. Therefore design optimization must take into account the impact of design parameters on the relative importance of the different heat transfer enhancement mechanisms and their attendant effect on pumping power.

Theoretical and computational investigations of flow and heat transfer in parallel-plate fin heat exchangers [1, 2] have often employed simplified models by assuming infinitesimally thin fins and steady laminar flow and thermal fields. By ignoring the finite thickness of the fin, such models have suppressed periodic shedding of the vortices and thereby account for only the boundary layer restart mechanism. Even studies which account for the finite fin thickness have often assumed the flow to be symmetric about the wake centerline and thereby obtained a steady laminar flow even at Reynolds numbers higher than the critical Reynolds number [4, 12]. Thus many of the previous theoretical models and numerical simulations have precluded much of the time-dependent flow physics and associated heat transfer enhancement and pumping power penalty.

With the rapid growth of computing power, large scale numerical simulations are becoming more realistic. It is now possible to obtain accurate time-dependent solutions with far fewer assumptions about the problems and to explore the full range of rich physics. For example, Ghaddar *et al.* [6] and Amon and Mikic [7] have solved the unsteady incompressible

¶ Author to whom correspondence should be addressed.

NOMENCLATURE

A_m	minimum flow cross-section area
b	fin thickness
C	transverse adjacent fin spacing
C_f	skin friction factor
D	computational domain
D_h	hydraulic diameter
$\hat{e}_x$	unit vector in streamwise, x, direction
f	friction factor
F	primary shedding frequency
H	half channel height in inline arrangement
j	modified Colburn factor
k	thermal conductivity of the fluid
L	fin length
L_x	computational domain length in x-direction
L_y	computational domain length in y-direction
$\hat{\mathbf{n}}$	outward normal unit vector on fin surface
Nu	Nusselt number
$\langle Nu \rangle$	global Nusselt number
ΔP	mean pressure difference
P	total pressure
p	modified perturbation pressure
Pr	Prandtl number, ν/α
Q	mean flow rate per unit spanwise width
q''	constant dimensional heat flux
Re	Reynolds number
s	length along the fin periphery
S	streamwise adjacent fin spacing
Str	Strouhal number
t	time
T	total temperature
$\mathbf{u}$	velocity in x- and y-directions, u, v
u_τ	friction velocity
V	mean flow velocity at A_m
W	spanwise width of the fin.

Greek symbols

α	fluid thermal diffusivity
β	mean pressure gradient
γ	mean temperature gradient
θ	modified perturbation temperature
$\mathscr{P}$	perimeters of fins within a basic unit
μ	fluid viscosity
ν	fluid kinematic viscosity
Ω_f	fin surface area.

Superscript

*	dimensional quantities.

Subscripts

f	based on fin
ref	based on reference
x, y	based on x, y Cartesian coordinates
τ	based on friction velocity.

Navier–Stokes and energy equations using the spectral element method to examine the unsteady flow and heat transfer in communicating and grooved channels. These studies have shown that the flow physics associated with flow separation at higher Reynolds numbers is too complex to be accounted for in steady-state computations.

In spite of these recent efforts, the details of the boundary layer restart and self-sustained oscillatory enhancement mechanisms have not been isolated and investigated in detail. In particular, in the context of parallel-plate fin heat exchangers a clear understanding of the individual roles of boundary layer restart and vortex shedding mechanisms on heat transfer and friction factor is lacking. Flow visualizations have shown that vortices roll up near the leading edge of the fins and subsequently travel downstream along the fin surface [13]. Von Karman vortices are also observed to form at the trailing edge of the fins and travel downstream in the wake before encountering the next fin element. A number of important issues regarding how the vortices are generated and how they interact with the parallel-plate fins still remain to be explored. Vortical flows are considered to enhance overall heat transfer [9, 10], but their impact on local heat transfer and skin friction in a compact heat exchanger needs to be quantified. Similarly the effect of wake vortex shedding on form drag needs to be quantified as well. Furthermore, the rate at which the strength of the leading edge vortex decreases as it travels over the fin surface is unclear, but such understanding will have significant impact on design parameters such as fin length and fin thickness.

The primary objective of the present study is to isolate the individual mechanisms through controlled numerical simulations in parallel-plate fin geometries. Two different arrangements of the parallel-plate geometry, inline and staggered, are investigated over a range of Reynolds numbers. At higher Reynolds numbers when the flow is naturally unsteady, along with the time-dependent simulations, corresponding steady-state simulations are performed by enforcing symmetry about the wake centerline. A comparison of the unsteady and steady symmetrized simulation results is used in exploring the unsteady enhancement mechanism due to vortex shedding. These results are further compared with the theoretical results for fully developed flow between uninterrupted continuous parallel plates and those of restarted boundary layers over fins of negligible thickness [1] in order to further

separate the role of boundary layer restart mechanism and the geometry effects arising from finite fin thickness and fin arrangement.

MATHEMATICAL FORMULATION AND PRELIMINARIES

In the present study we consider both inline and staggered parallel-plate fin arrangements which are shown in Fig. 1. In the inline arrangement fins of dimensional thickness, b^*, and length, L^*, form a periodic pattern with pitches L_x^* along the flow direction, x, and $L_y^* = 2H^*$ along the transverse direction, y. Thus the basic unit, indicated by the dashed line, contains a single fin. Here we consider a large array of this basic unit periodically repeated along the streamwise and transverse directions and Fig. 1(a) shows only nine basic units of this large array. Figure 1(b) shows the staggered arrangement which is obtained by offsetting fins IV, V and VI in Fig. 1(a) by half of L_x^* along the streamwise direction. The basic unit which now contains two fin elements, again marked by the dashed line, is periodically repeated along the streamwise and transverse directions. The heat transfer surface area per unit volume is the same for the two arrangements.

The governing equations solved in two-dimensions for the nondimensional velocity, $\mathbf{u}$, and temperature, T, fields are the Navier–Stokes and energy equations along with continuity, as shown below:

$$\frac{\partial \mathbf{u}}{\partial t} + \mathbf{u}\cdot\nabla\mathbf{u} = -\nabla P + \frac{1}{Re_\tau}\nabla^2\mathbf{u} \quad \text{in } D \tag{1}$$

$$\frac{\partial T}{\partial t} + \mathbf{u}\cdot\nabla T = \frac{1}{Re_\tau Pr}\nabla^2 T \quad \text{in } D \tag{2}$$

$$\nabla\cdot\mathbf{u} = 0 \quad \text{in } D \tag{3}$$

where D denotes the computational domain, indicated by the dashed line in Fig. 1 for each of the two cases. Here constant material properties along with negligible viscous dissipation and body forces have been assumed. In the above equations, the length and pressure scales are given by the half distance between adjacent fin rows along the transverse direction in the inline arrangement, H^*, and the applied dimensional pressure difference over a length of H^* along the streamwise direction, ΔP^*. The velocity scale is the friction velocity, $u_\tau^* = \Delta P^*/\rho)^{1/2}$. The temperature has been nondimensionalized by $q''^* H^*/k$, where q''^* is the specified dimensional constant heat flux on the fin surfaces. The above nondimensionalization results in two dimensionless parameters: Reynolds number based on friction velocity, $Re_\tau = u_\tau^* H^*/\nu$, and the Prandtl number which is here set to 0.7. In this paper we will primarily consider nondimensional quantities. Any use of dimensional quantities will be explicitly stated and denoted by a superscript (*) except that of constant material properties.

The present numerical solutions will assume periodicity of the solution over one basic unit and therefore the actual computational geometry will be limited to this basic unit [2, 4, 6, 7]. Thus, in an attempt to model the flow and heat transfer in a large periodic array of fin elements, the present computations ignore the entrance and exit effects.

To enable periodic boundary conditions, the nondimensional pressure will be split into a linear variation and a modified pressure as: $P = P_{in} - \beta x + p$, where P_{in} is the arbitrary nondimensional pressure at the inlet of the computational domain. The linear pressure variation will be chosen to fully account for the total pressure drop across the computational domain, which results in a nondimensional pressure gradient of $\beta = 1$. Thus the modified pressure, p, can

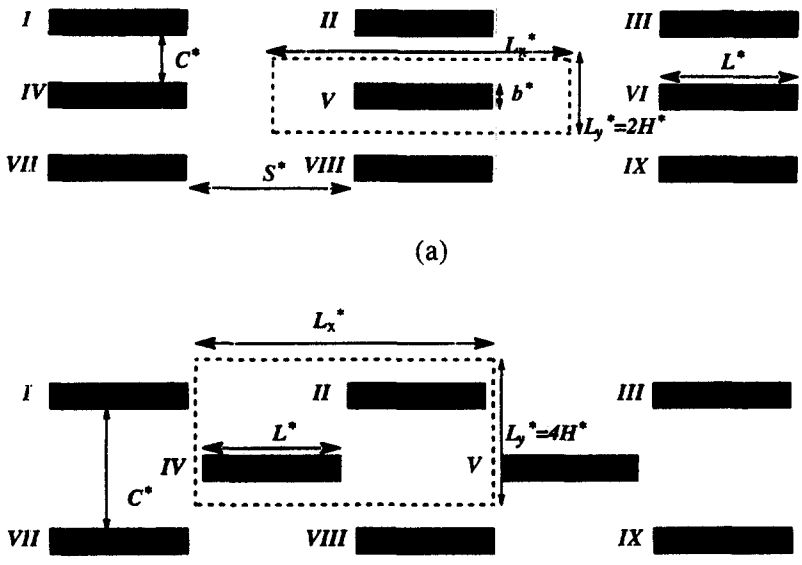

Fig. 1. Schematic of fin arrangement: (a) inline; (b) staggered. Fin numbers are marked in order to facilitate reference within the text and here $L^*/H^* = L = 6.4$, $L_x^*/H^* = L_x = 14.4$, $b^*/H^* = b = 0.75$, $S^*/H^* = S = 8$.

be assumed to be periodic over the computational domain. On the surface of the fin, no-slip and no-penetration conditions are imposed for the velocity field and Neumann type boundary condition of $\nabla p \cdot \hat{\mathbf{n}} = 0$ is applied for the pressure, where $\hat{\mathbf{n}}$ is the outward normal to the fin surface.

Similarly the nondimensional temperature, T, can be decomposed into a linear part and a modified nondimensional temperature, θ, as: $T(x, y, t) = T_{\text{in}} + \gamma x + \theta(x, y, t)$, where T_{in} is the arbitrary nondimensional inlet temperature and γx specifies the linear portion of the nondimensional temperature variation along the flow direction. This linear portion is so chosen that it fully accounts for the net temperature change from the inlet to the outlet of the computational domain. From an energy balance over the entire computational domain, γ can be expressed as $\gamma = \mathscr{P}/(Re_\tau PrQL_x)$, where $\mathscr{P}$ is the sum of the perimeters of fins within a basic unit. The modified temperature, θ, can then be considered to be periodic along both x and y directions. Since the temporal fluctuations in the flow rate are small, the corresponding fluctuations in γ are also small in magnitude [14]. The corresponding dimensional constant heat flux boundary condition on the fin surface is then given by $\nabla\theta \cdot \hat{\mathbf{n}} = 1 - \gamma \hat{\mathbf{e}}_x \cdot \hat{\mathbf{n}}$ for the modified nondimensional temperature, where $\hat{e}_x$ is the unit vector along the x direction.

Although the computations were performed with H^* and $(\nabla P^*/\rho)^{1/2}$ as the length and velocity scales, in the results to be presented the Reynolds number, Re, is defined based on the hydraulic diameter, $D_h^* = 4A_m^*/(\Omega_f^* L_x^*)$, as $Re = V^* D_h^*/\nu$, where V^* is the dimensional mean velocity at minimum flow cross-section area. In the inline arrangement shown in Fig. 1(a) the minimum flow cross-sectional area is chosen to be $(2H^* - b^*)W^*$ and the heat transfer surface area is $2(b^* + L^*)W^*$, while in the staggered arrangement shown in Fig. 1(b) the minimum flow cross-sectional area is chosen to be $(4H^* - 2b^*)W^*$ and the heat transfer surface area is $4(b^* + L^*)W^*$, where W^* is the width of the fin in the spanwise, z, direction, taken to be unity in the present two-dimensional simulations. Thus, for both the inline and staggered arrangements considered in the present computations the hydraulic diameters are given by $5.026H^*$. The Reynolds number defined here can be expressed in terms of nondimensional quantities as $Re = QD_h Re_\tau/(A_m/W)$.

Instantaneous local heat transfer will be expressed in terms of the instantaneous local Nusselt number based on hydraulic diameter and can be written in terms of nondimensional quantities as [14]:

$$Nu(s, t) = \frac{D_h}{\theta_f(s, t) - \theta_{\text{ref}}(s, t)} \tag{4}$$

where θ_{ref} is a reference nondimensional temperature defined as

$$\theta_{\text{ref}}(s, t) = \int \theta |u| \, dy \Big/ \int |u| dy.$$

Here the absolute value of the nondimensional streamwise velocity is used so that the regions with reversed flow are also properly represented [4]. Instantaneous global Nusselt number, $\langle Nu \rangle$, can be obtained through an integration around the fin surface [14]. The overall Nusselt number, denoted by $\overline{\langle Nu \rangle}$, is then defined as the average of the above over time. In order to evaluate the overall local heat transfer we also define the time averaged local Nusselt number, $\overline{Nu}(s)$, based on time averaged flow and thermal fields, $\bar{u}$ and $\bar{\theta}$ in eqn (4). In order to evaluate the overall performance of the system, a modified Colburn j factor and the friction factor, f, are defined as [14]:

$$j = \frac{\overline{\langle Nu \rangle}}{Re\, Pr^n} \quad \text{and} \quad f = \frac{D_h}{2} \frac{1}{(QW/A_m)^2} \tag{5}$$

where $n = 0.4$ for fully developed flow [3].

Here the governing equations are solved with all the relevant length and time scales adequately resolved and no turbulence models are employed. A second-order accurate control-volume formulation on a staggered grid with central difference approximation is employed [15]. The equations are integrated explicitly in time until a steady, periodic or a statistically stationary state is reached. For the inline fin arrangement, the periodic domain with one fin element is resolved with a grid of 128×32 grid cells. While in the staggered arrangement, the periodic domain with two fin elements is discretized with 256×64 grid cells. A grid dependence study showed that a 128×32 resolution per fin element predicted the j and f factors to within 5–10% of results on a 512×128 grid per fin element [14]. The computations were performed on a massively parallel Connection Machine 5, CM-5. A detailed description of the governing equations, periodic boundary conditions, numerical methodology and parallel performance can be found in Zhang *et al.* [14] and Tafti [16]. Detailed comparison of the results obtained from the present computational approach with those of corresponding experiments of Mullisen and Loehrke [5] and steady simulations of Sparrow and Liu [1] has been performed. The good agreement between the experimental and present computational results has also been reported in Zhang *et al.* [14].

RESULTS AND DISCUSSION

We begin by showing the various transitions undergone by the flow as the Reynolds number is increased in the inline and staggered arrangements of fins. Figure 2 shows the flow pattern and the corresponding time variation of the instantaneous global Nusselt number for the staggered geometry at four different Reynolds numbers: $Re = 246$, 720, 1245 and 1465. The constancy of $\langle Nu \rangle$ indicates that the flow is steady laminar at $Re = 246$. The recirculating bubble seen in the wake is observed to grow in size with increasing Reynolds number in the steady regime. The

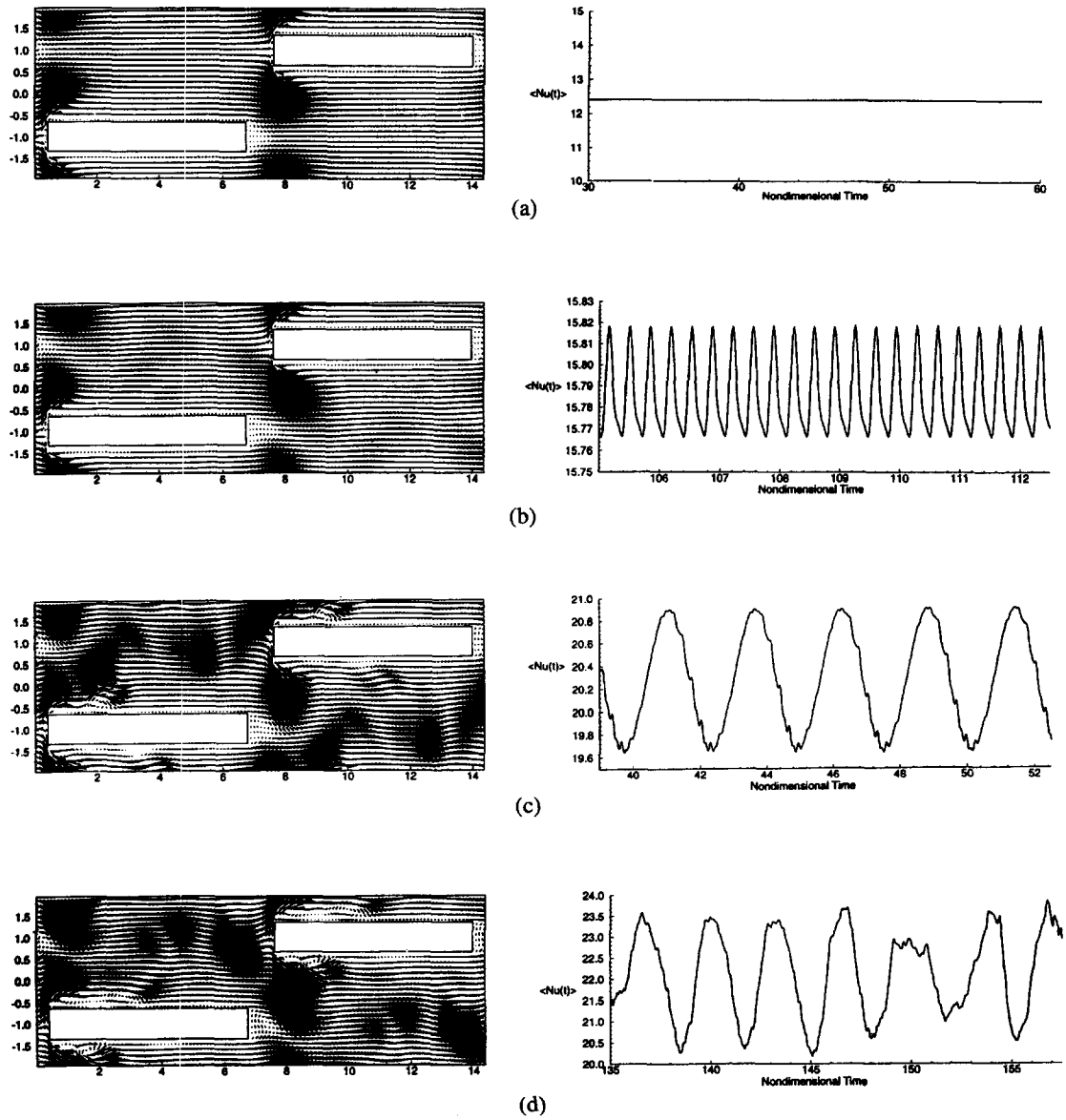

Fig. 2. Vector plot of velocity field and time trace of instantaneous global Nusselt number for the staggered arrangement: (a) $Re = 246$, the flow is steady; (b) $Re = 720$, the flow oscillates at a single frequency with a Strouhal number of 0.15; (c) $Re = 1245$, the Strouhal number of the primary frequency is 0.17, a secondary low frequency can also be observed; (d) $Re = 1465$, the flow is chaotic.

flow undergoes Hopf bifurcation at a critical Reynolds number somewhere between 474 and 720, which is consistent with theoretical prediction of a critical Reynolds number of 688 for this geometry [13]. Above this critical Reynolds number a time periodic state is obtained as can be inferred from the asymmetric state of the wake bubble and the small amplitude waviness of the wake at $Re = 720$. At this Reynolds number the time trace of the instantaneous global Nusselt number shows that the flow oscillates at a single frequency, with a Strouhal number $Str = 0.15$, where $Str = F^*b^*/V^*$ and F^* is the primary dimensional frequency of oscillation. As the Reynolds number further increases the flow undergoes another instability as can be seen from the appearance of a strong secondary low frequency in the time history of Nusselt number at $Re = 1245$. At this Reynolds number the Strouhal number of the primary frequency increases to 0.17 and the secondary low frequency is of magnitude of approximately 1/5 of the primary shedding frequency. Also can be seen is the appearance of well defined vortices that roll on the top and bottom surfaces of the fin. With further increase in Reynolds number the flow soon becomes chaotic as shown by the time history of Nusselt number at $Re = 1465$.

The flow in the inline arrangement follows a similar qualitative pattern, although the transition Reynolds numbers for the appearance of the various flow regimes quantitatively differ from those of the staggered arrangement. In the inline arrangement, the flow

Table 1. A list of nondimensional shedding frequency (*Str*), *j* factor, friction factor (*f*), percentile contribution to friction factor from skin friction and form drag at different Reynolds numbers for the inline arrangement

Re	*St*	*j*	*f*	Skin friction contribution	Form drag contribution
120	Steady	0.1655	0.4427	62.5%	37.5%
245	Steady	0.0843	0.2385	57.5%	42.5%
381	0.14	0.0577	0.1747	50.3%	49.7%
546	0.14	0.0436	0.1330	45.8%	54.2%
706	0.14	0.0363	0.1147	39.3%	60.7%
797	0.14	0.0332	0.1056	36.9%	63.1%
899	0.14	0.0305	0.0962	35.6%	64.4%
1128	0.14	0.0267	0.0799	34.4%	65.6%
1407	0.16	0.0260	0.0802	28.4%	71.6%
1669	0.16	0.0250	0.0820	23.1%	76.9%
1923	0.17	0.0242	0.0841	21.4%	78.6%
2191	0.17	0.0233	0.0846	19.0%	81.0%

Table 2. A list of shedding frequency (*Str*), *j* factor, friction factor (*f*), percentile contribution to friction factor from skin friction and form drag at different Reynolds numbers for the staggered arrangement

Re	*St*	*j*	*f*	Skin friction contribution	Form drag contribution
172	Steady	0.0761	0.1373	54.3%	45.7%
246	Steady	0.0582	0.1049	50.6%	49.4%
474	Steady	0.0338	0.0634	42.8%	57.2%
720	0.15	0.0253	0.0490	32.8%	67.2%
1018	0.16	0.0191	0.0383	24.5%	75.5%
1246	0.17	0.0188	0.0368	16.6%	83.4%
1465	0.17	0.0174	0.0362	13.2%	86.8%

remains steady for Reynolds numbers under approximately 350. Above this, up to a Reynolds number of about 2000, the flow is observed to be unsteady with a single shedding frequency. The appearance of an additional frequency and subsequent transitions to a chaotic state are delayed to higher Reynolds numbers compared with the staggered arrangement. The Strouhal numbers for both the inline and staggered arrangements are listed in Tables 1 and 2, respectively. In both cases, the Strouhal number, *Str*, can be seen to be nearly a constant over a range of Reynolds number and jumps to a higher value at a higher Reynolds number. Okajima [17] observed similar phenomena in his experiments on the vortex-shedding frequencies of various rectangular cylinders in a uniform flow. For the relatively high ratio of $L/b = 4$ employed in his experiments, Strouhal number is almost independent of Reynolds numbers and has a value of 0.14. Furthermore it is observed in Table 1 that there is a jump in Strouhal number near Reynolds number of 1400 and by analyzing the Fourier transform of the velocity field along the streamwise direction, it was confirmed that this jump is due to a discrete change in the number of waves observed along the streamwise direction. For the inline geometry, over the lower range of Reynolds number four waves were observed over a length of L_x and above a Reynolds number of 1400 five waves were observed, but the impact of the number of discretized waves on both global and local *j* and *f* factors at any given *Re* was not observed to be strong.

It must be pointed out that the flow and thermal fields in the unsteady regime are qualitatively similar in both arrangements. Figure 3(a) shows the instantaneous temperature contours for the staggered arrangement at $Re = 1465$ and the corresponding velocity vector field can be seen in Fig. 2(d). Figure 3(b–c) show the flow and thermal fields for the inline arrangement at a comparable Reynolds number of 1407. It is clear that in both arrangements there are vortices that roll on the top and bottom surfaces of the fin which significantly alter the local thermal field and thereby the local heat transfer. These vortices are clockwise rotating on the top surface and are anticlockwise rotating on the bottom surface. They act as large scale mixers and bring in fluid from the free-stream on their downstream side towards the fin surface and eject the fluid on their upstream side away from the fin surface. This can be seen to result in the crowding of the temperature contours near the fin surface. The oscillatory nature of the flow manifests itself in the wake of the fin elements as wavy motion that propagates in the streamwise direction over time.

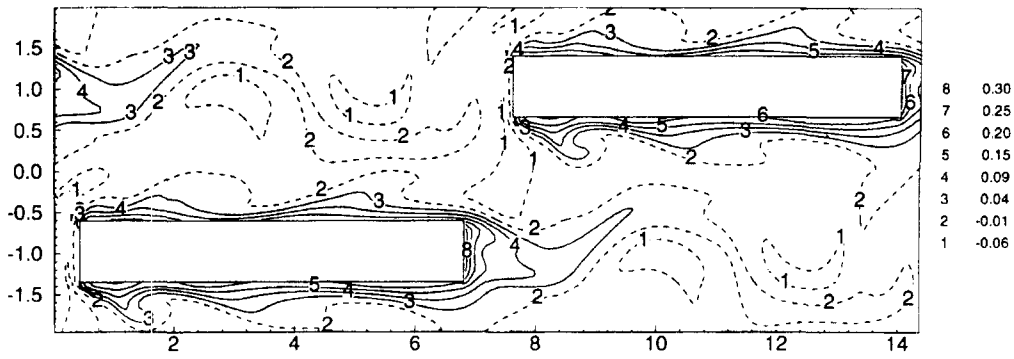

(a)

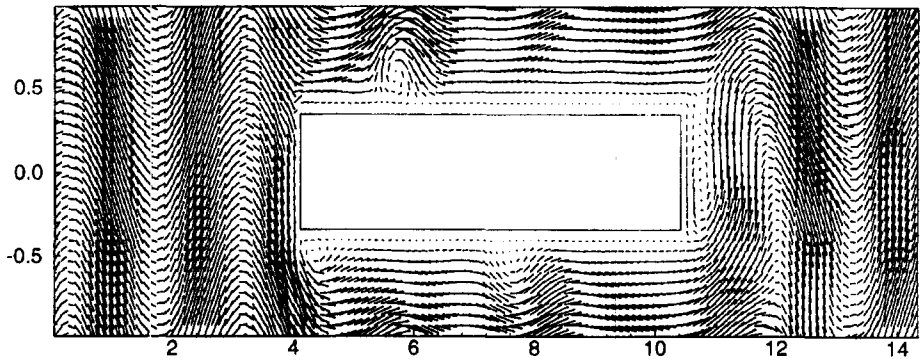

(b)

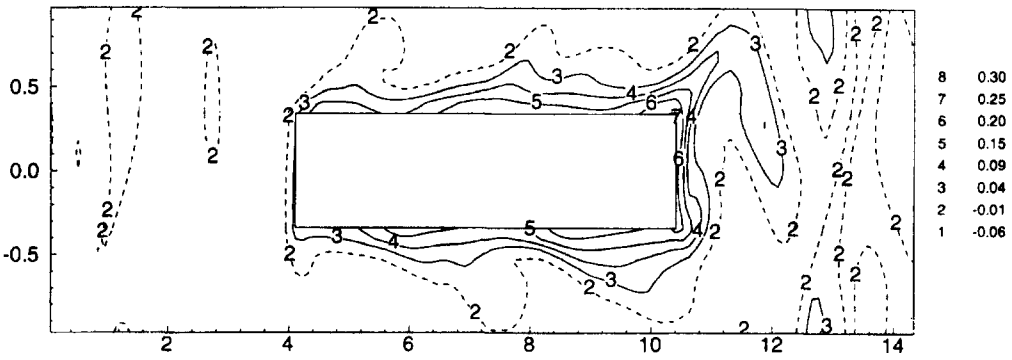

(c)

Fig. 3. Comparison of flow and thermal fields of the two arrangements: (a) contour plot of perturbation temperature for the staggered arrangement at $Re = 1465$ corresponding to the flow fields in Fig. 2(d); (b) vector plot of velocity field, (b) contour plot of perturbation temperature for the inline arrangement at $Re = 1407$.

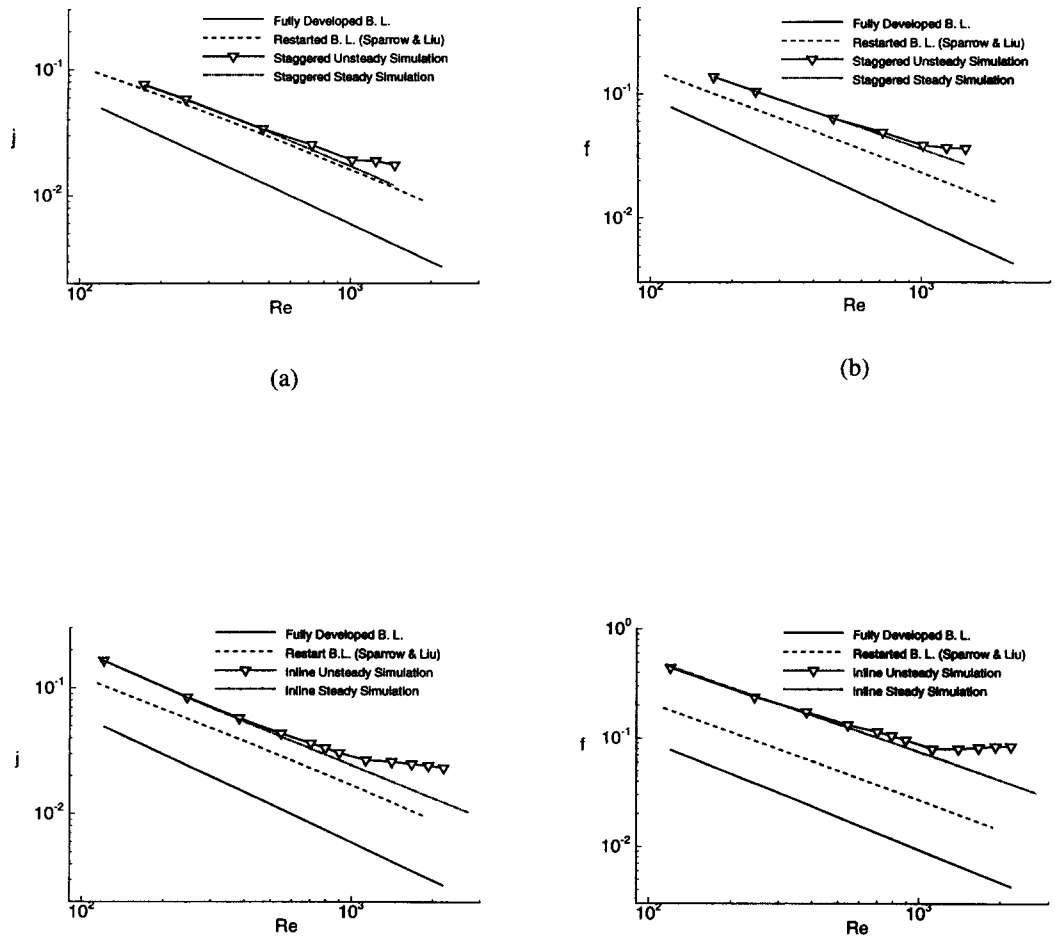

Fig. 4. A comparison of individual heat transfer enhancement mechanisms and their effect on frictional losses: (a) j factor; (b) friction factor for the staggered arrangement; (c) j factor; (d) friction factor for the inline arrangement.

Global results

In Fig. 4 the Colburn j factor and the friction factor, f, are plotted against Re on a log–log scale for both arrangements. Here the objective is to compare these results with those of Sparrow and Liu [1] and those for continuous parallel plates to isolate contributions to heat transfer and friction factor from the individual mechanisms. In order to make a fair comparison and proper estimation of the individual effects it is important to follow a uniform scaling of all the results. The theoretical results for the continuous flat plate, shown in Fig. 4 as the solid line, are based on a fully developed laminar flow and thermal fields between two infinitely long parallel plates with separation $4H^*$. This separation was chosen in order to maintain the heat transfer surface area per volume to be the same as in the inline or staggered arrangement. From Fig. 1, this corresponds to a continuous parallel plate formed by connecting fins I, IV, II, V, III and VI and so on, but with infinitesimal fin thickness.

The Nusselt number and the friction factor, based on half channel height, for a fully developed flow between parallel plates with constant heat flux are 35/17 and $1.5/Re$, respectively. In eqn (4), the Nusselt number for the inline and staggered arrangements has been defined as the ratio of actual heat transfer to corresponding conductive heat transfer with the hydraulic diameter as the length scale. Similarly in eqn (5) the friction factor represents the nondimensional losses over a streamwise length of D_h^*. For proper comparison, the j factor and friction factor along with Re must be defined with a single common length scale. Here we choose $D_h^* = 5.026H^*$, the hydraulic diameter of the inline and staggered arrangements as the common length scale (Sparrow and Liu use the hydraulic diameter of the continuous parallel plates as the com-

mon length scale [1]). This results in a scaling factor of $D_h/2$ and $D_h^2/4$ for the j factor and friction factor for the continuous parallel plate results. One then obtains the following j factor and friction factor relations

$$j = 6.0Re^{-1} \quad \text{and} \quad f = 9.4Re^{-1}$$

(continuous parallel plates) (6)

where Re is the Reynolds number for the parallel plates based on the hydraulic diameter. In the limit of flow between the continuous parallel plates, boundary layer restart and vortex shedding mechanisms are absent. Furthermore, the geometry effects arising from the finite thickness and the placement of the fin elements are absent as well. These three effects together account for the substantial increase in the computed j factor and friction factor over the continuous parallel plate results.

Also plotted as the dashed line in Fig. 4(a–b) are the results obtained by Sparrow and Liu [1] for the staggered arrangement. Once again, in order to maintain the heat transfer area the same, the dimensional transverse spacing between fin rows is maintained $2H^*$ and the dimensional fin length is half the computational domain ($L_x^*/2$). In their model the above two are the only parameters needed since it was assumed that the fins are infinitesimally thin and the resulting flow is considered to be steady. Their results on the j factor and friction factor are again converted with $D_h^* = 5.026H^*$ as the length scale and fit by a power law of the form:

$$j = 4.19Re^{-0.80} \quad \text{and} \quad f = 6.83Re^{-0.82}$$

(Sparrow and Liu, staggered). (7)

The difference between the continuous parallel plate and Sparrow and Liu's results accounts for only the effect of periodically restarting the hydrodynamic and thermal boundary layers. It is clear that the effect of boundary layer restart mechanism is to increase overall heat transfer but with the associated penalty of higher frictional loss.

It is still difficult to fully assess the importance of self-sustained flow oscillations because the difference between the present simulation results and those of Sparrow and Liu [1] also has contribution from the geometry effect, mainly arising from the finite thickness of the fin. In order to further isolate and separate these mechanisms, simulations were conducted in the same staggered arrangement shown in Fig. 1(b), but with appropriate symmetry imposed about the wake centerline. This symmetrization of the flow removes all asymmetry in the wake associated with the vortex shedding process and thus the flow is constrained to follow the steady solution. We shall call these symmetrized simulations as 'steady symmetrized simulations'. It can be seen that the steady symmetrized simulation also follows a power law behavior best fit by

$$j = 6.0Re^{-0.84} \quad \text{and} \quad f = 6.2Re^{-0.74}$$

(steady symmetrized staggered). (8)

Differences in the j and f factors of the steady symmetrized simulations and those of Sparrow and Liu [1] account for the finite thickness of the fin elements and the resulting steady wake bubble.

The finite thickness of the fin does seem to affect the overall heat transfer behavior a little, primarily due to the fact that the finite fin thickness decreases the transverse spacing available for the flow from $4H^*$ to $4H^* - b^*$. For the parameters shown in Fig. 1, this corresponds to a change of 18.75% in the transverse spacing. If this change in transverse spacing is accounted for, then the difference between the j factor of the steady symmetrized simulations and those of Sparrow and Liu [1] is negligible. This suggests that the other effects of finite fin thickness, such as those due to the wake bubble, can be ignored in heat transfer considerations, at least over the Reynolds number range considered here. Similarly, the decrease in transverse spacing available for the flow in the case of finite fin thickness accounts for most of the increase in the friction factor in the steady symmetrized simulations over the results of Sparrow and Liu [1]. Even with this change in transverse spacing account for, a noticeable increase in the friction factor can be observed. This increase can be attributed to the contribution to friction factor arising from the form drag, in case of finite fin thickness.

The results from unsteady simulations are identical to those from symmetrized steady simulations in the steady flow regime at low Reynolds numbers and follow the power law behavior, but above the critical Reynolds number, once the flow becomes time-dependent, the full simulation results show systematic deviation from the power law with significant increase in both the j factor and friction factor. Differences in the performance of the steady symmetrized and the unsymmetrized unsteady simulations is solely due to the effect of flow unsteadiness.

Figures 4(c–d) show the corresponding results for the inline fin arrangement. Here again a comparison of the j factor and friction factor from the continuous parallel plate theory, simulations of Sparrow and Liu [1] for inline plates of infinitesimal thickness, steady symmetrized simulations and the full unsteady simulations helps to separate the individual contributions from the boundary layer restart, finite geometry and self-sustained oscillatory effects. The results of Sparrow and Liu [1] and steady symmetrized simulations can be fit by the following power laws:

$$j = 6.06Re^{-0.85} \quad \text{and} \quad f = 12.73Re^{-0.89}$$

(Sparrow and Liu, inline) (9)

$$j = 10.5Re^{-0.88} \quad \text{and} \quad f = 22.5Re^{-0.82}$$

(steady symmetrized inline). (10)

The general trend seems to fit the description provided for the staggered arrangement. But there are some differences. Mainly, the geometry effect given by the difference between the steady symmetrized simulations and the results of Sparrow and Liu [1] appears larger than the staggered counterpart. This is because, in the inline geometry the effect of finite fin thickness in decreasing the transverse gap available for the flow from $2H^*$ to $2H^* - b^*$ accounts for a 37.5% reduction in the flow cross-section. Whereas, in the staggered arrangement the reduction in flow cross-section is only 18.75%. This decrease in the flow cross-section almost entirely accounts for the increase in j factor, but the friction factor is further increased by the presence of form drag in the case of finite fin thickness. Furthermore, in both the inline and staggered arrangements, the fully developed boundary layer results can be seen to slowly diverge off from the other two power laws with increasing Reynolds number. This effect is more visible in the friction factor. This is possibly due to the fact that at lower Reynolds numbers the flow between the adjacent plates in the transverse direction rapidly develops into a fully developed flow, whereas as the Reynolds number increases the entrance length for flow and thermal development also increases, thus increasing the deviation from a fully developed flow. This hypothesis will be confirmed later with a careful look at the hydrodynamic and thermal boundary layers.

Local Nusselt number distribution

In the following, the role of the vortices in enhancing the local heat transfer will be closely examined. Figure 5 shows the velocity vector field in the inline arrangement at $Re = 797$ at two different time instances and their corresponding instantaneous local Nusselt number distribution along the fin periphery. These two instances are separated by 0.5 non-dimensional time units, which corresponds to 0.45 shedding period. At the first time instance shown in Fig. 5(a) an anti clockwise vortex can be clearly seen to be located on the bottom left-hand side of the fin. Over time this vortex travels down the fin surface and at the later time instance shown in Fig. 5(b) it has significantly lost its strength and can be barely located at approximately $x = 7$ on the bottom surface. In the meantime a clockwise vortex has been shed off the front top leading edge of the fin and can be seen to be located at $x = 5$. In fact the imprint of an earlier clockwise vortex can be seen in Fig. 5(a) at $x = 8$ as the inrush of fluid towards the fin. Also marked in this figure are the fin surface locators starting from the top left corner (marked **A** in Fig. 5(b)) going around the clockwise direction (marked **B, C, D** in Fig. 5(b)) and back to the top left corner of the fin. These shed vortices act as large-scale mixers by entraining free-stream fluid around their downstream periphery and eject it upstream as observed by Tafti in flow over a blunt flat plate [18].

The local Nusselt number is significantly higher at the leading edge due to the stagnating nature of the flow, while it is significantly lower in the wake owing to the local recirculation. Enhancement in the local Nusselt number can be well correlated with the presence of clockwise and anti clockwise vortices. For example the anti clockwise vortex seen in Fig. 5(a) at $x = 5$ can be seen to generate a strong local peak in the Nusselt number at $s = 12.2$. At the later instance, this vortex has moved downstream to $x = 6.7$ ($s = 10.5$) and its impact on local Nusselt number has decreased. Similarly the clockwise vortex on the top surface of the fin can be also related to a local peak in the Nusselt number variation and it can be inferred that the vortices can increase local Nusselt number by as much as 50%. Also plotted in Fig. 5(c) are the time-averaged local Nusselt number, $\overline{Nu}(s)$, for the unsteady simulation and the local Nusselt number obtained from the corresponding steady symmetrized simulation at approximately the same Reynolds number ($Re = 804$). In the case of the steady symmetrized solution the monotonic decrease in the Nusselt number away from the front leading edge is solely due to the growth in the thermal boundary layer. In the case of time-dependent simulations, significant improvement in local heat transfer can be attributed to the presence of vortices. The vortices can be seen to adversely affect local Nusselt number on their upstream end where fluid is pushed away from the fin surface and result in a local decrease in the Nusselt number below the steady symmetrized simulation result. On the other hand, an increase in the local Nusselt number is realized at the downstream side of the vortex where fluid is brought to the fin surface, which more than compensates for the decrease at the other upstream end. The net effect is to increase heat transfer over the entire fin surface in the time-dependent flow regime.

Figure 6 shows the time-averaged Nusselt number distribution on the top (or bottom) surface of the fin for many different Reynolds numbers for both arrangements. In the inline arrangement, at lower Reynolds numbers below 700, the Nusselt number distribution can be seen to decay to an asymptotic value of 16.56. This asymptotic value is the theoretical Nusselt number corresponding to a hydrodynamically and thermally fully developed flow between parallel plates of separation $C^* = 2H^* - b^*$ (see Fig. 1(a)) with isoflux boundary conditions, converted appropriately for the present hydraulic diameter of the inline arrangement. Thus it can be seen that at the lowest Reynolds number considered ($Re = 120$) the thermal boundary layer grows to within 1% of the fully developed thermal boundary layer profile within the first 33% of the fin surface ($s < 2.1$). As Reynolds number increases, the Nusselt number at the leading edge grows and increasingly departs from the asymptotic value. Accordingly the length of the thermal entrance region also increases and eventually grows beyond the length of the fin. Therefore, at higher Reynolds numbers the Nusselt number even at the

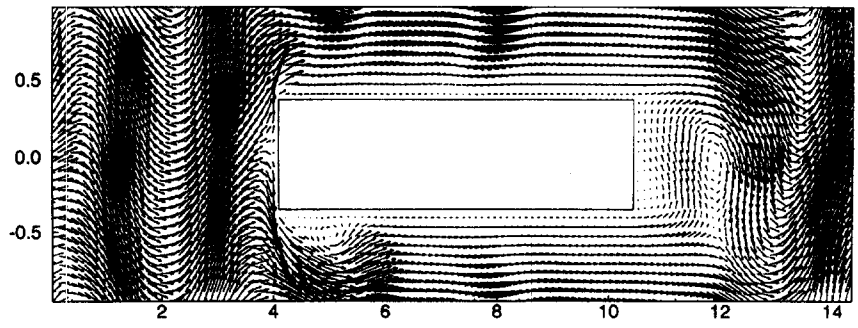

(a)

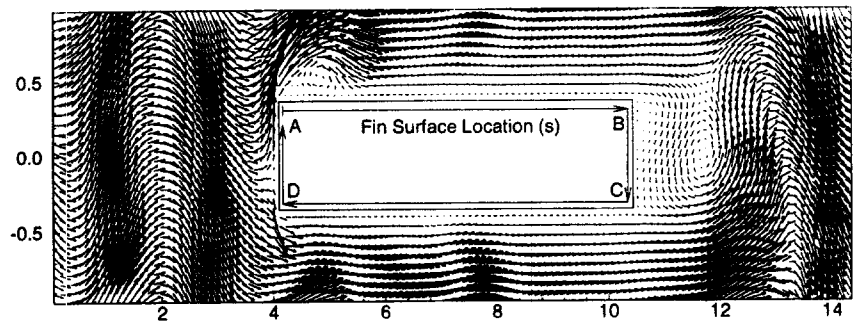

(b)

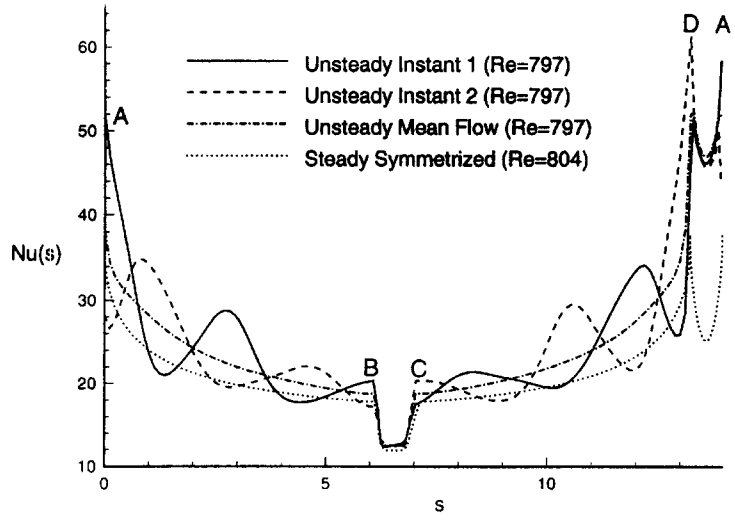

(c)

Fig. 5. Vector plot of instantaneous velocity fields for the inline arrangement at $Re = 797$ and local Nusselt number distribution: (a) instance 1; (b) instance 2, approximately 0.5 nondimensional time units after instance 1; (c) local Nusselt number distribution.

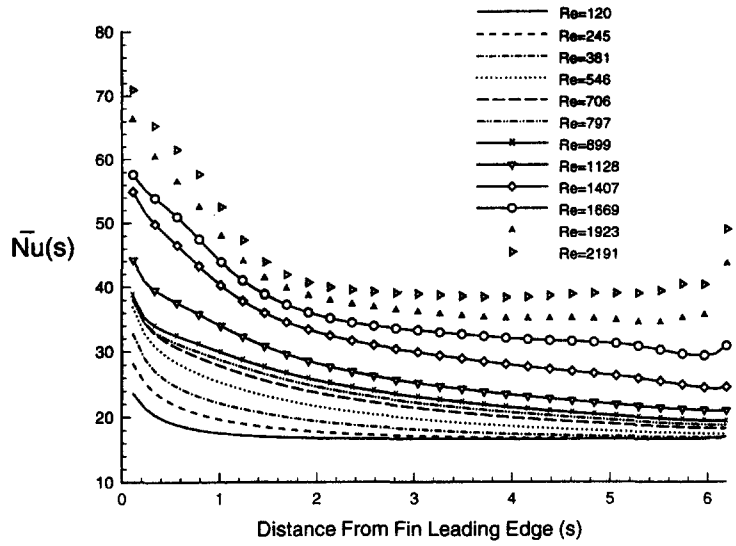

(a)

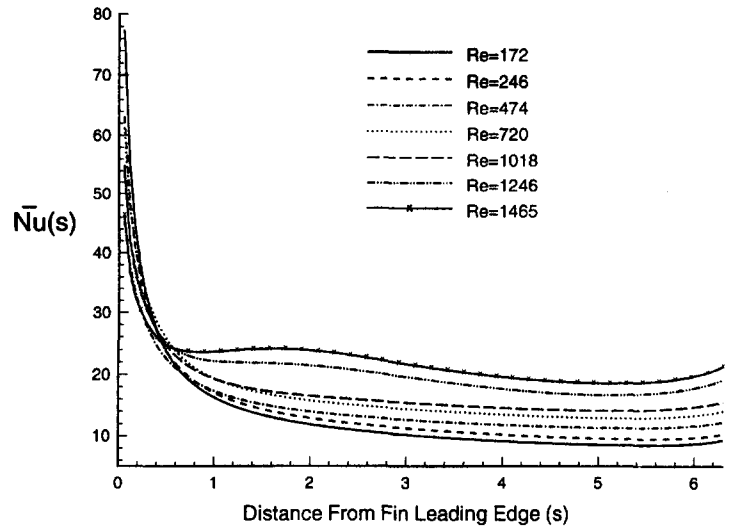

(b)

Fig. 6. Time-averaged Nusselt number distribution on top fin surface: (a) in inline arrangement; (b) in staggered arrangement.

trailing edge is appreciably greater than 16.56. At higher Reynolds numbers in the time-dependent flow regime, the Nusselt number distribution does not exhibit a simple decay as at lower Reynolds numbers. A change in the Nusselt number distribution due to the strong influence of the leading edge vortices on the upstream portion of the fin surface can be clearly seen. Although the general behavior in the staggered arrangement can be inferred to be qualitatively the same as that of the inline arrangement, there are a number of differences which warrant further comment. At the lower Reynolds numbers when the flow is steady, the local Nusselt number can be seen to approach an asymptotic value of 6.37, which corresponds to the theoretical Nusselt number for a hydrodynamically and thermally fully developed flow between parallel plates of separation $C^* = 4H^* - b^*$ (see Fig. 1 (b)) with isoflux boundary conditions, con-

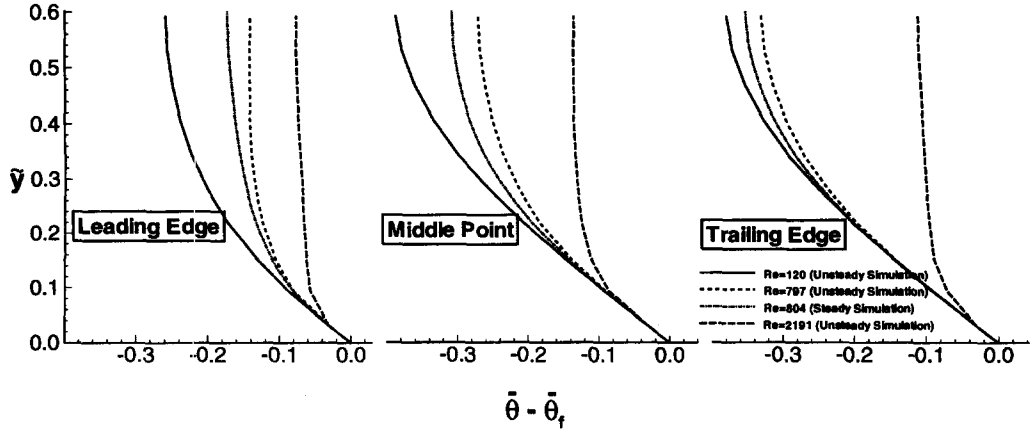

(a)

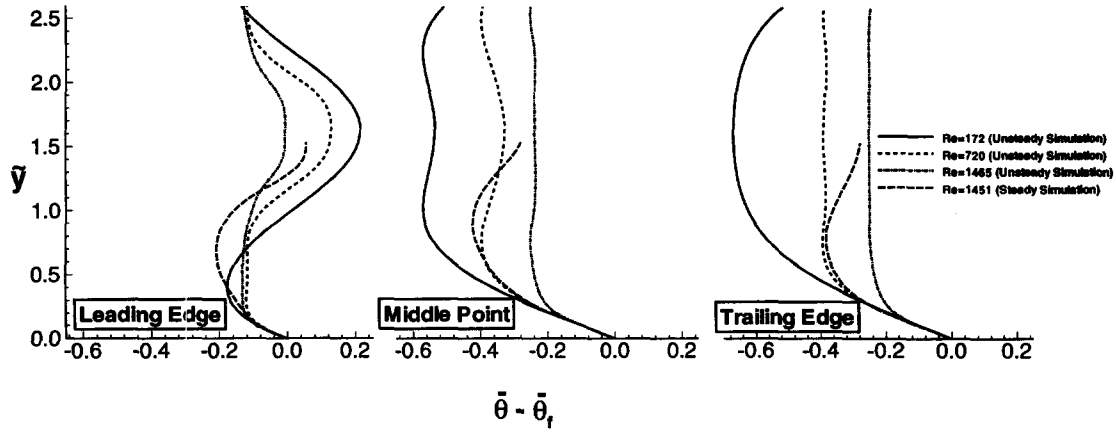

(b)

Fig. 7. Time-averaged temperature difference as a function of distance away from the fin surface at three different streamwise locations: (a) in inline arrangement; (b) in staggered arrangement.

verted appropriately for the present hydraulic diameter definition of the staggered arrangement. This asymptotic value of fully developed Nusselt number is only 38.5% of that of the inline arrangement, since the transverse spacing between the fin elements in the inline arrangement is proportionately smaller than the staggered arrangement, but unlike the inline arrangement, the approach to this asymptotic value is not complete by the trailing edge even at the lowest Reynolds number. This is due to the fact that the velocity and temperature profiles at the leading edge are quite distorted and strongly influenced by the upstream fin elements in the staggered arrangement (see Fig. 7(b)). This effect can also be seen in the significantly higher local Nusselt number near the leading edge of the fin. As Reynolds number increases, interestingly the local Nusselt number at the leading edge decreases due to the effect of the wake of the upstream fin elements. Whereas, away from the leading edge over most of the fin surface the local Nusselt number increases with increasing Reynolds number, owing to the action of unsteady vortices. Just like in the inline geometry, systematic deviations from a simple exponential decay can be observed at the higher Reynolds numbers due to contribution from strong vortices.

The time-averaged nondimensional temperature difference, $\bar{\theta}-\bar{\theta}_f$, profiles as a function of distance away from the fin surface, $\tilde{y}$, are plotted in Fig. 7 at

different Reynolds numbers for both arrangements. In inline arrangement, results for the unsymmetrized full simulations at $Re = 120$, 797 and 2191 are plotted at three different locations on the fin surface: at the leading edge, middle of the top (or bottom) surface of the fin and at the trailing edge of the fin, so that the development of the profile can be clearly observed. Also plotted at a Reynolds number close to 797 are the corresponding temperature difference profiles for the steady symmetrized simulation at $Re = 804$. In the present simulations, since the heat flux at the fin surface is held fixed, the nondimensional temperature gradient at the fin boundary ($\tilde{y} = 0$) always remains the same (equal to unity). Therefore, from the Nusselt number definition given in eqn (4), it can be seen that larger the deviation of the free stream temperature from the local fin surface temperature, the lower will the corresponding time-averaged local Nusselt number. The lower freestream temperature at $Re = 120$ indicates a corresponding lower Nu. At this lowest Reynolds number the temperature profile quickly develops into a fully developed thermal profile and very little difference exists between the thermal profiles at the mid-point of the fin and at the trailing edge. At the intermediate Reynolds number the time-averaged thermal profile slowly develops till the trailing edge of the fin. On the other hand, at $Re = 2191$ the time-averaged thermal profiles indicate a rapid decrease in the time-averaged local Nusselt number from the leading edge to the mid-point of the fin, but a small increase in $\overline{Nu}(s)$ towards the trailing edge. These results are consistent with the time-averaged local Nusselt number distributions shown in Fig. 6(a).

Comparing the $\bar{\theta} - \bar{\theta}_f$ profiles at $Re = 797$ with those of the corresponding steady symmetrized simulation at $Re = 804$, the effect of vortices on increasing the time-averaged fluid temperature to approach the fin surface temperature can be seen over the entire fin length. This effect can be seen to somewhat decrease towards the trailing edge, possibly due to the weakening of the vortices as they travel downstream. Furthermore, the steady symmetrized solution suggests that even in the absence of vortex shedding the thermal profile is not fully developed by the trailing edge at higher Reynolds numbers. This is in full agreement with theoretical results that entrance length increases with Reynolds number in the laminar regime [19].

Figure 7(b) shows similar plots for staggered arrangement for three different Reynolds numbers, $Re = 172$, 720 and 1465. Also plotted at the highest Reynolds number is the corresponding temperature difference profile for the steady symmetrized simulation at approximately the same Reynolds number ($Re = 1451$). All these profiles are plotted over only half the domain in the transverse, y, direction and the profile over the other half can be obtained by symmetry. It can be clearly seen that even at the lowest Reynolds number the temperature profile does not develop into a fully developed thermal profile by the trailing edge. At the leading edge, the influence of the wake of the upstream fin element appears as the significant temperature reversal away from the fin surface. This reversal is particularly strong at the lowest Reynolds number, since the size of thermal wake is bigger at lower Reynolds number, as can be observed from the trailing edge profiles. This results in a significantly reduced difference between the fin surface and mixed mean fluid temperature and explains the higher local Nusselt number near the leading edge at lower Reynolds numbers. Comparing the $\bar{\theta} - \bar{\theta}_f$ profiles at $Re = 1465$ with those of the corresponding steady symmetrized simulation at $Re = 1451$, it can be observed that the effect of time-dependent vortices is to bring the fluid temperature closer to the fin surface temperature over the entire fin length.

Local skin friction distribution

In this section the effect of vortex shedding on friction factor will be investigated. In the case of fins with finite thickness the friction factor derives contributions both from the skin friction on the top and bottom surfaces of the fin and from the form drag due to the pressure difference between the front and back surfaces of the fin. In Tables 1 and 2, the total friction factor, percentile contribution to friction factor from skin friction and percentile contribution from form drag are listed for the inline and staggered arrangements, respectively. In both geometries the percentile contribution from skin friction steadily decreases with increasing Reynolds number, while the form drag becomes increasingly important. This result is in agreement with our common knowledge of bluff body wakes. Among the two arrangements, the form drag is relatively more important in the staggered arrangement than in the inline arrangement. This again is consistent with our expectation that the percentile contribution from the form drag to be lower in the inline arrangement since geometrically each fin is sheltered by the wake of the upstream fin array. It is important to note that, while at lower Reynolds numbers there is near equal partition between the skin friction and form drag contributions, at higher Reynolds number the form drag contribution is factor four or more greater than the skin friction contribution.

Figure 8 investigates the effect of the vortices that roll on the top and bottom surfaces of the fin on local skin friction factor. Here local skin friction factor is defined as,

$$C_f = \frac{\mu}{H^*}\left[\frac{\partial u^*}{\partial y^*}\right]_{\text{wall}} \frac{D_h^*}{2\rho V^{*2}},$$

consistent with the overall friction factor defined in eqn (5) which includes contribution from form drag as well. The local skin friction factor on the top surface of the fin at $Re = 797$ for the inline arrangement is plotted in Fig. 8(a) at two different time instances shown in Fig. 5(a–b). The corresponding local Nusselt number were presented earlier in Fig. 5(c). It can be

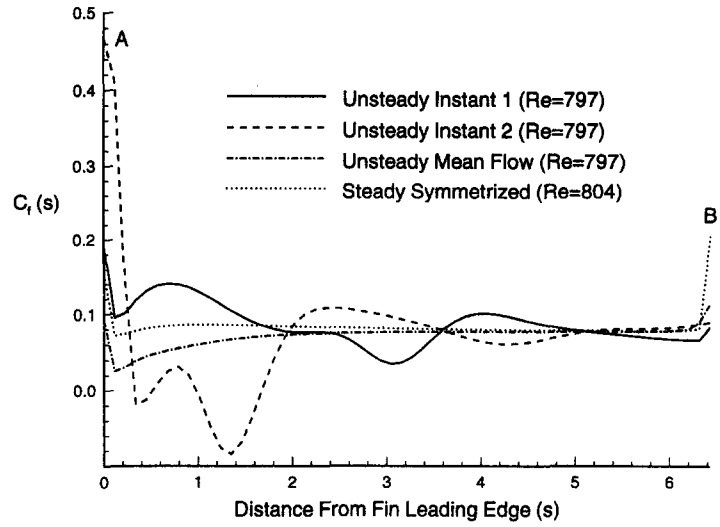

(a)

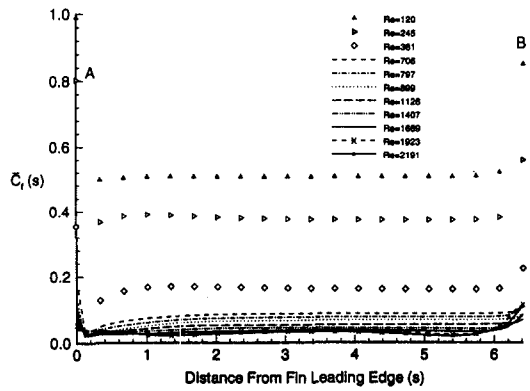

(b)

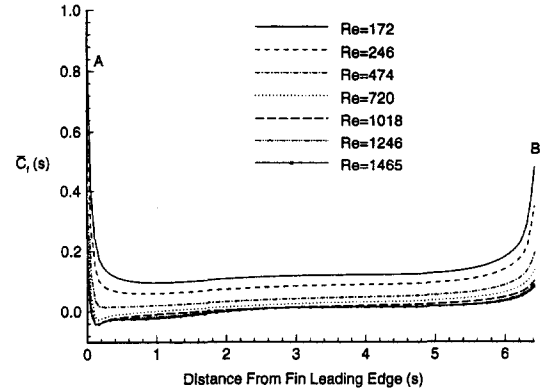

(c)

Fig. 8. Local skin friction factor distribution along top fin surface: (a) instantaneous skin friction factor inline arrangement corresponding to the flow fields shown in Fig. 5; (b) mean skin friction factor in inline arrangement; (c) mean skin friction factor in staggered arrangement.

clearly seen by comparing the C_f distribution with the vortex seen near the leading edge in Fig. 5(b), that the effect of the vortex for the most part is to decrease the local skin friction. In fact, due to the local reversed flow induced by the vortex a negative skin friction, corresponding to a negative drag force, can be seen. The weaker local maximum and minimum around $s = 0.8$ and $s = 0.4$ suggest the presence of smaller counter rotating eddies (which are not large enough to be fully visible in Fig. 5(b)) at the heel of the larger clockwise rotating vortex. Downstream of the vortex, the skin friction factor quickly becomes positive and approaches a near constant value of about 0.08. The effect of the vortices can also be seen as the local minimum at $s = 3.1$ in the local skin friction factor distribution at the earlier time corresponding to Fig. 5(a), but the drop in C_f is not as dramatic due to the rapid decay of the vortices as they travel downstream.

Also plotted in this figure are the time-averaged local skin friction factor, $\bar{C}_f(s)$, for the unsteady simulation and the local skin friction factor obtained from the corresponding steady symmetrized simulation at $Re = 804$. A comparison of the instantaneous distributions with the time averaged distribution clearly illustrates the strong effect of the vortices in decreasing local C_f by as much as 64% near the leading edge. Of course, this effect significantly weakens downstream. The decrease in the local skin friction factor obtained in the time-dependent simulation over the corresponding steady state simulations can be attributed

to the presence of vortices. Thus the effect of the vortex on skin friction can be seen to be just the opposite of its effect on local Nusselt number. Although the above results are for the inline arrangement, an investigation of the staggered arrangement shows similar strong local reduction in the skin friction factor due to the vortices.

Figure 8(b) shows the time-averaged local skin friction factor for all the Reynolds numbers of the inline arrangement. At the lowest Reynolds number of 120, the skin friction factor can be seen to decay to an asymptotic value of about 0.505. This asymptotic value is in full agreement with the theoretical friction factor of $60.63/Re$ corresponding to a fully developed parabolic flow between parallel plates of separation $C^* = 2H^* - b^*$, converted appropriately for the present hydraulic diameter definition. Thus it can be seen that the boundary layer grows very rapidly to the fully developed profile. At slightly higher Reynolds numbers, the effect of the finite fin thickness can be seen as the undershoot very close to the leading edge in the approach to the asymptotic value. Furthermore the approach to the asymptotic value appears very rapid and not strongly dependent on the Reynolds number. This appears to be in contradiction to the theoretical prediction that the entrance length for the development of the hydrodynamic boundary layer in a channel increases linearly with Reynolds number [19]. But it will soon be noted that the velocity profile even at the leading edge is close to a parabolic profile and significantly different from a plug flow assumed in the theory. The rapid increase in the friction factor close to the trailing edge is due to the sudden expansion of the flow downstream of the trailing edge.

Figure 8(c) shows the corresponding time-averaged $C_f(s)$ for the staggered arrangement. The behavior of the skin friction factor appears to be similar to that of the inline arrangement except for two noticeable differences. First, at lower Reynolds numbers the friction factor now asymptotes to a lower value given by $17.94/Re$, which corresponds to the theoretical value for a fully developed parabolic velocity profile between parallel plates of separation $C^* = 4H^* - b^*$, converted appropriately for the present hydraulic diameter definition. Second, at Reynolds numbers greater than 720, the time-averaged skin friction factor is negative near the leading edge indicating the presence of a separated flow region in the time-averaged mean flow. Such a reversed flow region was absent in the time-averaged mean flows of inline arrangement. This indicates a stronger influence of the vortices in the staggered arrangement. The length on the mean reversed flow region can be seen to increase with Re and the increase is rapid at lower Reynolds number. The difference between these profiles is very small at higher Reynolds numbers, which suggests the possibility of a self similar time-averaged C_f distribution independent of Reynolds number. Such approach to self similarity can also be observed for the inline arrangement.

The time-averaged streamwise velocity profiles as a function of distance away from the fin surface, $\tilde{y}$, are plotted in Fig. 9 for both arrangements at different Reynolds numbers. In the inline arrangement, results for the unsymmetrized full simulations at $Re = 120$, 797 and 2191 are plotted at three different locations on the fin surface: at the leading edge, middle of the top (or bottom) surface of the fin and at the trailing edge of the fin, so that the downstream development of the hydrodynamic boundary layer can be followed. Also plotted at a Reynolds number close to 797 ($Re = 804$) are the corresponding $\bar{u}$ profiles for the steady symmetrized simulation. As pointed out earlier the approaching velocity profile at the leading edge is so close to the final fully developed parabolic velocity profile that the hydrodynamic entrance length is small. Comparison of the velocity profiles at $Re = 797$ with those of the corresponding steady symmetrized simulation at $Re = 804$ is not straightforward. Since the overall friction factor for the unsteady simulation is larger, the corresponding time-averaged flow rate is 8.5% smaller than that of the steady symmetrized flow (note that in the present simulations the non-dimensional pressure drop is held fixed in all the simulations). Thus part of the decreased local skin friction factor in the unsymmetrized simulation over the steady symmetrized simulation observed in Fig. 8(a) is due to this decreased time-averaged flow rate. This difference in flow rate is sufficient to account for the difference at the mid-point of the fin and further downstream, whereas the larger difference close to the leading edge is clearly due to the action of the vortices. While the unsteady flow phenomenon at higher Reynolds numbers is thus seen to decrease the skin friction contribution, its effect on form drag is just the opposite. The form drag increases with flow oscillation and more than compensates for the decrease in skin friction and thereby the overall friction factor is increased over the steady symmetrized simulation.

Similar plots for the staggered arrangement at three different Reynolds numbers: $Re = 172$, 720 and 1465 are shown in Fig. 9(b). Also plotted are the corresponding streamwise velocity profiles for the steady symmetrized simulation at $Re = 1451$. All these profiles are plotted over only half the domain in the transverse, y, direction. At the leading edge, the wake of the upstream, fin element appears to strongly influence the velocity profile. A sharp decrease in the streamwise velocity at $\tilde{y} = 1.625$ (midway between the adjacent fin elements) accounts for the significant departure from a parabolic profile. This decrease in the local velocity near the centerline somewhat increases the maximum velocity in order to conserve flow rate and furthermore the location of the maximum velocity moves closer to the fin surface (e.g. $\tilde{y} \approx 0.4$ at $Re = 172$). This results in a significantly increased velocity gradient at the fin surface and explains the higher local skin friction coefficient near the leading edge. It can be clearly seen that even at the lowest Reynolds number the velocity profile does not develop into a

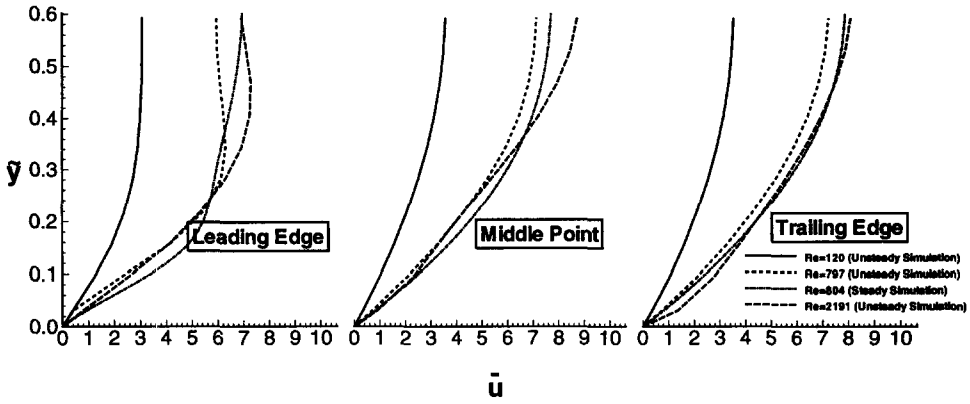

(a)

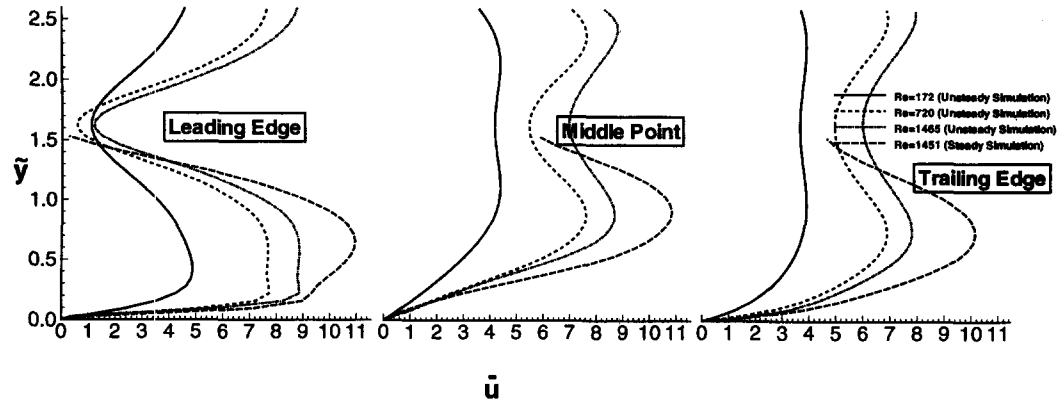

(b)

Fig. 9. Time-averaged streamwise velocity profiles as a function of distance away from the top fin surface at three different streamwise locations: (a) in inline arrangement; (b) in staggered arrangement.

fully developed parabolic profile by the trailing edge. Comparing the velocity profiles at $Re = 1465$ with those of the corresponding steady symmetrized simulation at $Re = 1451$, it can be observed that due to the increased overall friction factor the unsteady simulations result in a 15% smaller time-averaged flow rate than the steady symmetrized simulations. The lower flow rate contributes to a lower skin friction coefficient in case of the unsteady simulations, and more importantly the effect of the vortices in the unsteady regime is to further decrease the skin friction contribution, but as seen in the inline arrangement, the effect of time-dependent flow oscillation is to significantly increase the form drag and more than compensate for the decrease in the skin friction contribution.

CONCLUSION

Here we have employed numerical simulations to explore the fluid flow and heat transfer in parallel-plate heat exchangers in the time-dependent flow regime and this approach has proven to be a very powerful tool in understanding the associated rich physics. The effects of vortex shedding and the associated flow unsteadiness have been captured by solving the unsteady Navier–Stokes and energy equations in two-dimensions. The flow field is assumed to be periodic along the streamwise and transverse directions in order to simulate flow over a large array of identical fin elements. The constant heat flux boundary condition employed in the present simulation allows for periodic boundary condition to be applied for a modified temperature field. Both inline and staggered arrangement of fins are considered and results obtained from these simulations are compared with those obtained from continuous parallel plates and the steady simulations of Sparrow and Liu [1] on inline and staggered flat fins of infinitesimal thickness.

The inline and staggered arrangements are seen to increase heat transfer and friction factor over a cor-

responding continuous parallel plate geometry with a plate separation of $4H^*$ (which maintains the same heat transfer surface area). The boundary layer restart and the geometry effects act in significantly different ways in the inline and staggered arrangements. In the case of inline arrangement the transverse gap between adjacent fins (C^*—see Fig. 1(a)) available for through flow is more than halved. Thereby the velocity and temperature gradients are increased resulting in significant increase in the j and f factors. But the velocity and temperature profiles approaching any fin element are not too far disturbed from the fully developed parabolic profile. In the case of staggered arrangement, the transverse gap between adjacent fin elements, $C^* = 4H^* - b^*$, decreases only slightly due to the finite thickness of the fin. On the other hand, owing to the staggered arrangement the velocity and temperature profiles approaching any fin element are significantly distorted away from the fully developed profile. The resulting increased velocity and thermal gradients at the fin surface contribute to increased j and f factors. At higher Reynolds numbers, in both these arrangements the time-dependent flow modulation due to vortex shedding further significantly enhances heat transfer with associated pumping power increase.

Irrespective of the fin arrangement the flow is observed to follow a sequence of transitions. At very low Reynolds numbers the flow is steady and above a critical Reynolds number flow becomes unsteady with a single dominant frequency. At even higher Reynolds numbers an additional lower frequency is generated and with subsequent increase in Re the flow becomes chaotic. In the inline arrangement these transitions are observed at a higher Reynolds number than in the staggered arrangement, but in both arrangements the unsteady regime is marked by vortices that are generated at the leading edges of the fin element, which travel down on the top and bottom surfaces of the fin element. These vortices play a key role in significantly enhancing the local heat transfer by bringing fresh fluid from the freestream towards the fin surface. On the other hand, the reversed flow generated by the vortices near the fin surface is responsible for an overall reduction in skin friction on the fin surface.

The overall friction factor receives contribution from the form drag as well due to the wake behind the trailing end of the fin element. It is observed that the flow unsteadiness manifests itself in the wake as waviness induced by vortex shedding and this significantly increases the form drag contribution. Since the increase in form drag is greater than the decrease in skin friction, the overall drag also increases due to time-dependent flow motion. This raises an interesting possibility that if vortices that roll on the fin be enhanced but the waviness in the wake be suppressed, enhanced heat transfer may be achieved without pumping power penalty. It must be pointed out that the vortex shedding on the front leading edges and flow waviness in the wake are intimately related, with each influencing the other. This is a line of thought that is worth pursuing in order to improve the overall performance of the heat exchanger.

Acknowledgement—This research was performed under a grant from the Air Conditioning and Refrigeration Center (ACRC) at the University of Illinois at Urbana-Champaign and the computation time was provided by the National Center for Supercomputing Applications (NCSA) on the massively parallel CM-5. The authors would like acknowledge Ms N. C. DeJong and Professor A. M. Jacobi within the Department of Mechanical and Industrial Engineering at the University of Illinois at Urbana-Champaign for many insightful discussions, comments and suggestions.

REFERENCES

1. Sparrow, E. M. and Liu, C. H., Heat transfer, pressure-drop and performance relationships for inline, staggered and continuous plate heat exchangers. *International Journal of Heat and Mass Transfer*, 1979, **22**, 1613–1624.
2. Patankar, S. V., Liu, C. H. and Sparrow, E. M., Fully developed flow and heat transfer in ducts having streamwise-periodic variations of cross-sectional area. *Journal of Heat Transfer*, 1977, **99**, 180–186.
3. Sparrow, E, M. and Hajiloo, A., Measurements of heat transfer and pressure drop for an array of staggered plates aligned parallel to an air flow. *Journal of Heat Transfer*, 1980, **102**, 426–432.
4. Patankar, S. V. and Prakash, C., An analysis of the effect of plate thickness on laminar flow and heat transfer in interrupted-plate passages. *International Journal of Heat and Mass Transfer*, 1981, **24**, 51–58.
5. Mullisen, R. S. and Loehrke, R. I., A study of the flow mechanics responsible for heat transfer enhancement in interrupted-plate heat exchangers. *Journal of Heat Transfer*, 1986, **108**, 377–385.
6. Ghaddar, N. K., Karniadakis, G. E., Patera, A. T., A conservative isoparametric spectral element method for forced convection; application to fully developed flow in periodic geometries. *Numerical Heat Transfer*, 1986, **9**, 277–300.
7. Amon, C. H. and Mikic, B. B., Spectral element simulations of unsteady forced convective heat transfer: application to compact heat exchanger geometries. *Numerical Heat Transfer, Part A*, 1991, **19**, 1–19.
8. Manglik, R. M. and Bergles, A. E., Heat transfer and pressure drop correlations for the rectangular offset strip fin compact heat exchangers. *Experimental Thermal Fluid Science*, 1995, **10**, 171–180.
9. Jacobi, A. M. and Shah, R. K., Heat transfer surface enhancements through the use of longitudinal vortices: a review of recent progress. *Experimental Thermal Fluid Science*, 1995, **11**, 295–309.
10. Valencia, A., Fiebig, M. and Mitra, N. K., Heat transfer enhancement by longitudinal vortices in a fin-tube heat exchanger element with flat tubes. *Journal of Heat Transfer*, 1996, **118**, 209–211.
11. Mittal, R. and Balachandar, S., Effect of three-dimensionality on the lift and drag of circular and elliptic cylinders. *Physics Fluids*, 1995, **7**, 1841–1865.
12. Suzuki, K., Hirai, E., Miyaki, T. and Sato, T., Numerical and experimental studies on a two-dimensional model of an offset strip-fin type compact heat exchanger used at low Reynolds number. *International Journal of Heat and Mass Transfer*, 1985, **28**, 823–836.
13. Joshi, H. M. and Webb, R. L., Heat transfer and friction in the offset strip-fin heat exchanger. *International Journal of Heat and Mass Transfer*, 1987, **30**, 69–84.
14. Zhang, L. W., Tafti, D. K., Najjar, F. M. and Balachandar, S., Computations of flow and heat transfer in parallel-plate fin heat exchangers on the CM-5; effects

of flow unsteadiness and three-dimensionality. *International Journal of Heat and Mass Transfer*, 1997, **40,** 1325–1341.
15. Harlow, F. J. and Welch, J. E., Numerical calculation of time-dependent viscous incompressible flow of fluid with free surface. *Physics Fluids*, 1965, **8**(12), 2181–2189.
16. Tafti, D. K., Comparison of some upwind-biased high-order formulations with a second-order central-difference scheme for time integration of the incompressible Navier–Stokes equations. *Computers and Fluids*, 1996, **25**(7), 647–665.
17. Okajima, A., Strouhal numbers of rectangular cylinders. *Journal of Fluid Mechanics*, 1982, **123,** 379–398.
18. Tafti, D. K., Vorticity dynamics and scalar transport in separated and reattached flow on a blunt plate. *Physics Fluids, A*, 1991, **5**(7), 1661–1673.
19. White, F. M., *Viscous Fluid Flow*. McGraw-Hill, New York, 1974, Chap. 4.